



Cite this: DOI: 10.1039/c8tc02979b

## Deciphering the potentiometric properties of (porphinato)zinc(II)-derived supramolecular polymers and related superstructures†‡

Chuan Liu,  Kaixuan Liu, Jared Klutke, Adam Ashcraft, Samantha Steefel and Jean-Hubert Olivier \*

Because modulating the structure–function relationships of  $\pi$ -conjugated superstructures opens fresh opportunities to tune the electronic structures of semiconducting materials, self-assembled architectures have emerged as pivotal candidates to engineer optoelectronic devices. While the photophysical and electrical properties of 1-dimensional supramolecular polymers have been extensively explored, establishing their fundamental potentiometric properties using reliable electrochemical measurements has been less scrutinized and would benefit the engineering of semiconducting materials. In this regard, elucidating the energy level of valence and conduction bands that delineate the electronic structure of self-assemblies is critical to unveiling the parameters that regulate their structure–function properties. In the present contribution, design principles to engineer 2-dimensional nanosheets, nanowires, fibers and amorphous solids from (porphinato)zinc(II) (PZn) building blocks have been elucidated by modifying the structural properties of the side chains that flank PZn-based cores. As these self-assemblies feature identical redox-active building blocks but evidence different solid-state morphologies, the elucidation of their potentiometric properties reveals important structural parameters that regulate the potentials at which holes and electrons are injected into the valence and conduction bands of these hierarchical materials. While self-assembly conformations modestly impact valence band energies, superstructures built from H-type aggregates feature a conduction band energy stabilized by more than 350 meV with respect to those constructed from J-type aggregates.

Received 17th June 2018,  
Accepted 6th August 2018

DOI: 10.1039/c8tc02979b

rsc.li/materials-c

## Introduction

Controlling the aggregation of  $\pi$ -conjugated building blocks to construct well-defined nano-to-mesoscale semiconductors fuels interest in applications such as light energy transduction,<sup>1–7</sup> charge transport,<sup>8–12</sup> and spintronics.<sup>13–16</sup> For example, programming the assembly of 1-dimensional (1D) superstructures at the molecular level has provided new platforms with which to not only deepen the understanding of light–matter interaction but also to manipulate the flow of excitons and charge carriers.<sup>17–22</sup> The emergence of electronic properties evidenced in organic superstructures that feature stacks of redox-active  $\pi$ -conjugated units traces its genesis from the interaction of frontier molecular orbitals of each building block that ultimately enforces the formation of new energy levels and spectroscopic

states.<sup>23</sup> In this regard, benchmark theoretical studies have unambiguously demonstrated the cardinal role played by superstructure conformation in delineating their electronic properties whereas minor modification of repeating unit registry can drastically impact the electronic coupling between building blocks.<sup>24–27</sup>

Advances in supramolecular chemistry have unraveled important design principles that have led to the creation of hierarchical materials equipped with appealing structure–function properties relevant to energy capture, conversion, and storage.<sup>28</sup> The elucidation of the mechanisms that govern formation of 1D and 2-dimensional (2D) supramolecular polymers (SPs) has provided fresh opportunities to modulate the electronic properties of these materials.<sup>29–33</sup> For example, pioneering works have demonstrated the selective assembly of (porphinato)zinc(II) and perylene diimide building blocks into H-aggregates and J-aggregates by manipulating the pathway complexity that regulates the formations of these supramolecular polymers.<sup>34–44</sup> In addition, investigation of the excited state of 1D supramolecular polymers using pump–probe time-resolved spectroscopy in the nanosecond and femtosecond time domains has unveiled exciton delocalization length and charge carrier generation.<sup>45–48</sup>

Department of Chemistry, University of Miami, Cox Science Building,

1301 Memorial Drive, Coral Gables, 33146, USA. E-mail: jh.olivier@miami.edu

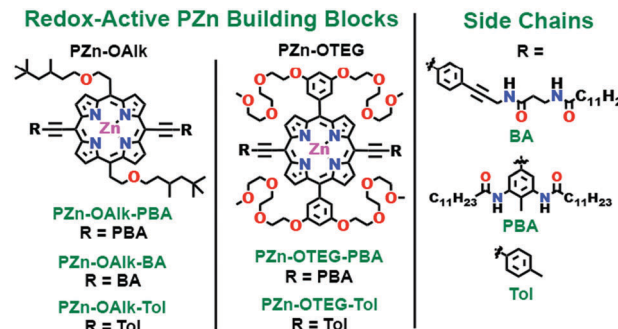
† This paper is dedicated to Margot. Welcome to the world little girl.

‡ Electronic supplementary information (ESI) available: Synthesis, characterization and aggregation mechanisms of redox-active building blocks. AFM, absorption spectra, NMR, IR, MS, and cyclic voltammetry. See DOI: 10.1039/c8tc02979b

Undeniably, developing strategies to fine tune the optical properties of  $\pi$ -conjugated aggregates is critical for the engineering of electro-optical devices.

While the photophysical and electrical properties of 1D supramolecular polymers have been vastly investigated, elucidation of their potentiometric properties using reliable electrochemical measurement methods and internal references has attracted less attention. It is important to note that exciton dissociation and free-charge carrier recombination are processes that regulate the performance of optoelectronic devices and they are intimately related to the valence and conduction band energies of semiconducting materials.<sup>18,49</sup> In this regard, it is critical to develop a fundamental understanding of the potentiometric properties that characterize supramolecular polymers to illuminate the structural parameters that regulate the energies of valence and conduction bands for this class of self-assembled semiconductors. Electrochemical techniques have been well-exploited to reliably determine the redox potentials of covalent semiconducting polymers and, most recently, semiconducting carbon nanotubes.<sup>50,51</sup> In the present contribution, we elucidate the potentiometric properties of semiconducting superstructures using cyclic voltammetry experiments. By exploring the electronic structure of hierarchical materials built from (porphinato)zinc(II) cores, we demonstrate that conformation of organic self-assemblies significantly modulates the valence and conduction band energies.

Because of their unique optical and electronic properties,<sup>52–57</sup> porphyrin-based chromophores have been extensively studied in solution and in the solid state, and they have been successfully exploited as light-harvesting and charge transport media in a plethora of electro-optical devices.<sup>58,59</sup> The elucidation of parameters that govern formations of some supramolecular polymers built from porphyrin-based units as unique building blocks has only recently been reported;<sup>34–38</sup> it is worth noting that only a handful of studies have investigated the structure–function properties of porphyrin-derived supramolecular polymers. To gain a deeper understanding of the electronic properties of porphyrin-derived SPs, the three building blocks **PZn-OAlk-PBA**, **PZn-OAlk-BA** and **PZn-OTEG-PBA** presented in Scheme 1 have been engineered and their self-assembly mechanisms were elucidated using temperature-dependent aggregation study. Side chains that flank each (porphinato)zinc(II) unit feature amide functional groups well-recognized to engender the formation of non-covalent interactions by means of hydrogen bonding.<sup>60</sup> In addition, to further explore the self-assembly energy landscape, modification of the porphyrin cores by introducing 3,5-bis(triethyleneglycoxy)phenyl substituents at the 10,20-positions equips the **PZn-OTEG** building block with amphiphilic character. Exploiting atomic force microscopy, we demonstrate that the morphology of superstructures built from drop-casted solution can be regulated as a function of precursor properties. While supramolecular polymers formed by temperature-induced self-assembly show 1D fiber-like materials and 2D nanosheets, elementary 1D nanowires can self-construct in the solid state by drop-casting solubilized building blocks. Redox potential measurements performed on these hierarchical materials have unveiled important structure–function properties. For identical redox active cores, a drastic



Scheme 1 Molecular structures of the (porphinato)zinc(II) building blocks exploited to construct hierarchical self-assemblies. Detailed synthesis protocols can be found in the ESI.† Please note that racemic functional groups have been utilized to synthesize **PZn-OAlk**-based building blocks.

stabilization of the conduction band energy is evidenced for 1D nanowires when compared to fiber-like compositions and suggests that parameters such as the screening effect must be considered when probing the conduction and valence band energies of semiconducting self-assemblies.

## Results and discussion

Self-assembly mechanisms of **PZn-OAlk-PBA**, **PZn-OAlk-BA**, and **PZn-OTEG-PBA** building blocks have been elucidated by temperature-dependent aggregation experiments chronicled in Fig. 1. For all experiments, porphyrin solutions were heated at the indicated temperature to ensure that building blocks are fully individualized. Ground state electronic absorption spectrum recorded for **PZn-OAlk-PBA** at 100 °C in 9% DMF in toluene features a sharp B-band at 453 nm and Q-band absorption centered at 664 nm ( $\epsilon = 20\,000\text{ M}^{-1}\text{ cm}^{-1}$ ;  $f = 0.100$ ) that are spectral attributes of individualized (porphinato)zinc(II) chromophores. The descent to 0 °C is accompanied by: (1) decrease of the B-band oscillator strength ( $f_{100^\circ\text{C}} = 0.638 \rightarrow f_{0^\circ\text{C}} = 0.167$ ), (2) the concomitant rise of novel absorptive features centered at 430 and 409 nm, (3) a  $371\text{ cm}^{-1}$  hypsochromic shift of the Q-band transition. Taken together, these emergent spectral signatures suggest the formation of H-type aggregate upon cooling. To elucidate the assembly mechanism that governs the aggregation of **PZn-OAlk-PBA** building blocks, the degree of aggregation ( $\alpha$ ) as a function of temperature was calculated following eqn S1 (ESI†) and is presented as inset in Fig. 1a. The observed sigmoidal shape is characteristic of an isodesmic supramolecular polymerization mechanism. Fitting the data using the model developed by van der Schoot<sup>61</sup> (see ESI†) provides an elongation chain constant of  $3.5 \times 10^5\text{ mol}^{-1}$ , and a change of enthalpy  $\Delta H_e = -80.71\text{ kJ mol}^{-1}$  that accompanied the supramolecular polymerization process.

The self-assembly mechanism of **PZn-OAlk-BA** building blocks recorded in toluene ( $c = 6.5 \times 10^{-6}\text{ M}$ ) contrasts that elucidated for **PZn-OAlk-PBA** and underscores the cardinal role played by the structural side chains that flank the redox active sub-units. The ground state electronic absorption spectrum recorded at 110 °C features spectral signatures characteristic of individualized **PZn-OAlk-BA** building blocks: (1) intense

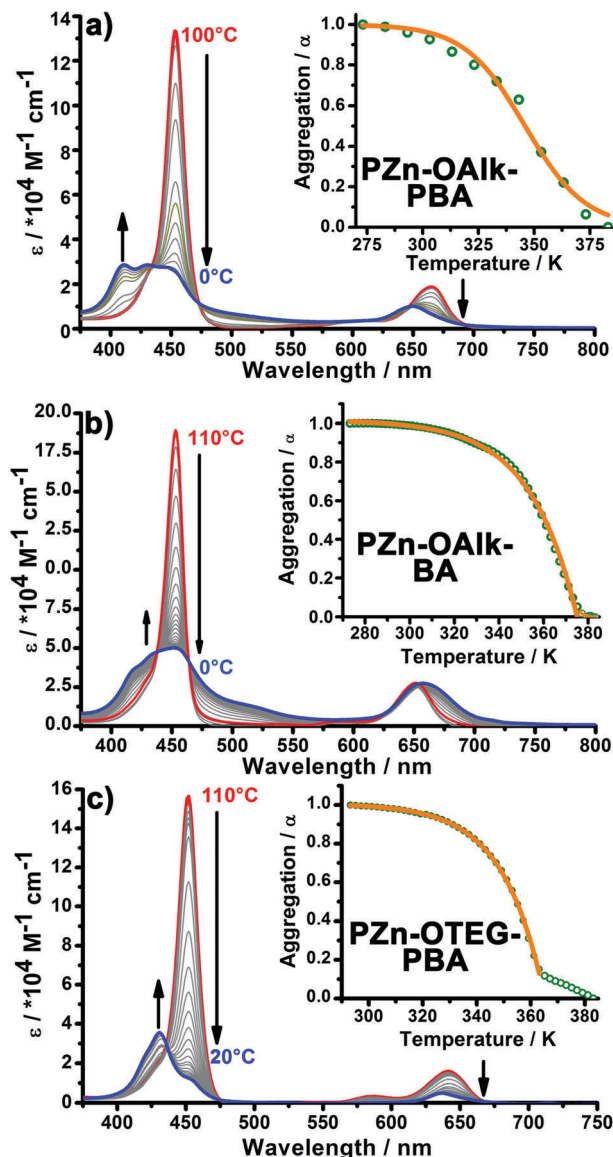


**Fig. 1** Ground-state electronic absorption spectra that chronicle the aggregation of PZn-derived building blocks as a function of temperature. (a) **PZn-OAlk-PBA** building blocks in 9% DMF in toluene solution,  $c = 5.7 \times 10^{-5}$  M, optical path length = 2 mm; (b) **PZn-OAlk-BA** building blocks in toluene solution,  $c = 6.5 \times 10^{-6}$  M, optical path length = 10 mm; (c) **PZn-OTEG-PBA** building blocks in toluene solution,  $c = 4.7 \times 10^{-6}$  M, optical path length = 10 mm. For all measurements, a cooling rate of  $1 \text{ K min}^{-1}$  was utilized. Insets in all the panels correspond to the degree of aggregation ( $\alpha$ ) as a function of temperature calculated from the attenuation of the extinction coefficient at 453 nm (green circles); the orange lines represent the resulting fits using the temperature-dependent isodesmic (a) and cooperative model (b and c).

porphyrin-derived B-band absorption centered at 453 nm and associated with an oscillator strength of 0.830, and (2) a dominant porphyrin-derived Q-band absorption centered at 651 nm ( $\epsilon = 27\,300 \text{ M}^{-1} \text{ cm}^{-1}$ ;  $f = 0.0917$ ). Drastic perturbations of these spectral attributes can be diagnosed upon cooling to  $0^\circ\text{C}$ : (1) decrease of the B-band oscillator strength ( $f_{100^\circ\text{C}} = 0.830 \rightarrow f_{0^\circ\text{C}} = 0.515$ ), and (2) the apparition of new absorptive

features centered at 417, 434, and 517 nm in addition to a  $411 \text{ cm}^{-1}$  bathochromic shift of the Q-band transition. These spectral signatures indicate the formation of J-type aggregate. A close examination of the curve that relates degree of aggregation ( $\alpha$ ) as a function of temperature reveals a non-sigmoidal shape characterized by an abrupt increase of aggregation below a specific temperature. These aggregative properties are reminiscent of a nucleation–elongation mechanism that regulates the formation of supramolecular **PZn-OAlk-BA** polymers. It is worth noting that the average length of the stack ( $N$ )  $T_e$  at the critical elongation temperature  $T_e = 102^\circ\text{C}$  corresponds to a dimer intermediate that evolves toward a supramolecular polymer built from 150 repeating units at  $0^\circ\text{C}$  (see ESI† for detailed explanation). The elongation process is associated with a change of enthalpy  $\Delta H_e = -55.1 \text{ kJ mol}^{-1}$ .

When compared to **PZn-OAlk-PBA**, the amphiphilic character conferred by the four pendant triethylene glycol side chains featured on the **PZn-OTEG-PBA** building block impacts the aggregation mechanism that regulates formation of supramolecular **PZn-OTEG-PBA** polymer. While at  $110^\circ\text{C}$ , **PZn-OTEG-PBA** units exist as individualized building blocks as evidenced by the absorption spectrum recorded in toluene ( $c = 4.7 \times 10^{-6} \text{ M}$ ) and presented in Fig. 1c, excursion to room temperature favours the formation of H-type aggregate confirmed by the hypsochromic shift of the Q-band from 642 nm to 636 nm in addition to the formation of novel absorptive features on the blue edge of the B-band at 419 nm ( $\epsilon = 20\,650 \text{ M}^{-1} \text{ cm}^{-1}$ ;  $f = 0.175$ ) and 431 nm ( $\epsilon = 29\,200 \text{ M}^{-1} \text{ cm}^{-1}$ ;  $f = 0.157$ ). Despite the fact that the shape of the curve displaying the degree of aggregation as a function of temperature (inset, Fig. 1c) suggests a nucleation–elongation mechanism, fitting the data using the conventional cooperative model has revealed unsuccessful. Surprisingly, while the elongation regime can be successfully treated exploiting the well-accepted van der Schoot model,<sup>61</sup> the nucleation process differs to some extent from the conventional uphill cooperative model. The linear increase of degree of aggregation as a function of temperature may suggest a nucleation step that processes through a downhill mechanism model.<sup>62</sup>

To further investigate the role played by porphyrin-derived precursors in regulating final superstructure conformations, AFM was utilized to scrutinize the solid-state morphologies of drop-casted porphyrin solutions. Fig. 2 and 3 are representative AFM images that chronicle the structural properties of drop-casted **PZn-OAlk-PBA**, **PZn-OAlk-BA** and **PZn-OTEG-PBA** porphyrin precursors. Please note that the following discussion compares morphologies of solid-state materials constructed by exploiting individualized PZn unit and supramolecular PZn polymer as primary building blocks. Unambiguously demonstrated by ground-state electronic absorption spectroscopy, **PZn-OAlk-PBA** building blocks in DMF solution remain individualized at room temperature (see Fig. S1, ESI†) while temperature treatment of a 9% DMF in toluene solution enables formation of supramolecular polymer compositions. These conformational discrepancies elucidated in solution transpire as well in the solid state as underscored when comparing Fig. 2a and b. When deposited from a DMF solution, **PZn-OAlk-PBA** building blocks interact along a 1D axis

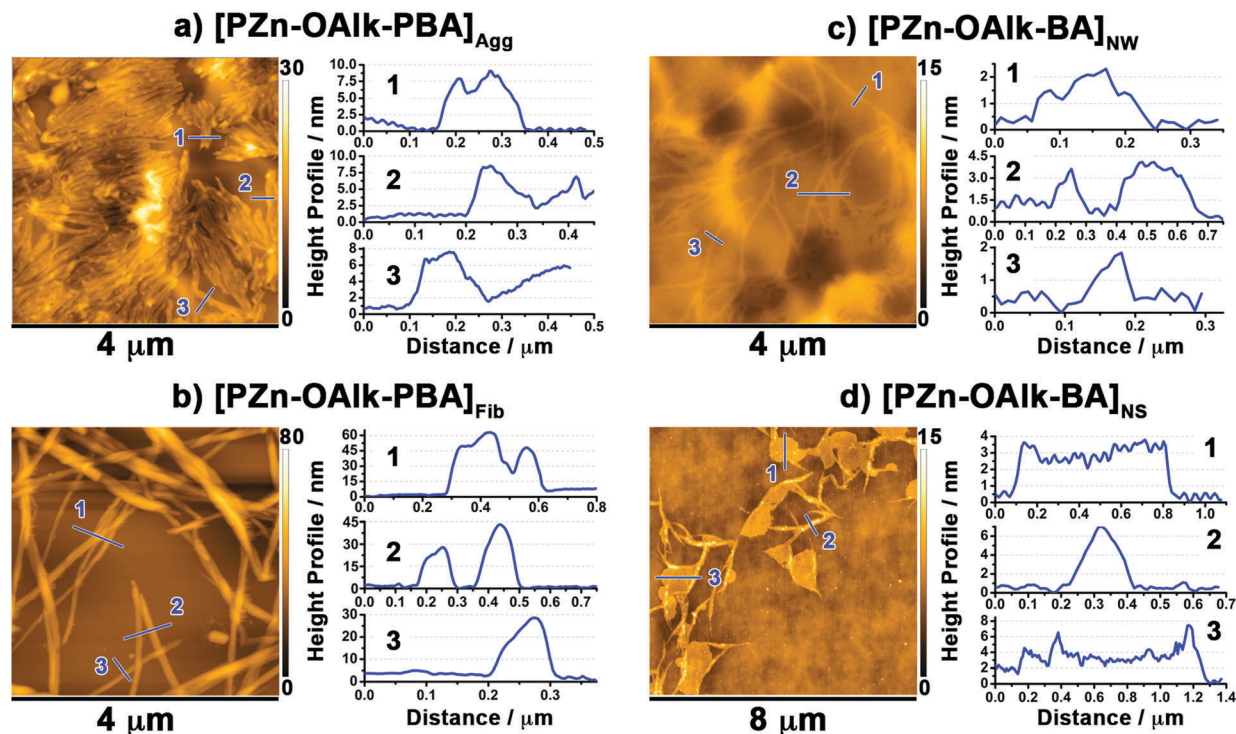


Fig. 2 Topographic intermittent contact mode AFM acquired and associated height profiles recorded for drop-casted: (a)  $[\text{PZn-OAlk-PBA}]_{\text{Agg}}$  aggregates that originate from individualized PZn-derived building blocks in DMF solution; (b)  $[\text{PZn-OAlk-PBA}]_{\text{Fib}}$  fibers constructed from parent PZn-derived supramolecular polymer in 9% DMF in toluene solution; (c)  $[\text{PZn-OAlk-BA}]_{\text{NW}}$  nanowires built from individualized PZn-derived building blocks in DMF solution; (d)  $[\text{PZn-OAlk-BA}]_{\text{NS}}$  nanosheets engineered from parent PZn-derived supramolecular polymer in toluene. For each panel, the height profile corresponds to the associated numbers on the AFM images.

parallel to the surface plane to form solid-state compositions best described by flattened “rod-like” assemblies with lengths that vary from 200 nm to 2  $\mu\text{m}$ .

The height profile ranging from 7.5 to 10 nm combined with DFT calculation performed on molecular  $\text{PZn-OAlk-PBA}$  construct (Fig. S26, ESI $\ddagger$ ) indicates that 2 to 3 PZn repeating units laterally interact to delineate the multi-layered assembly. The fact that initially individualized  $\text{PZn-OAlk-PBA}$  building blocks spontaneously assemble into materials with a non-negligible degree of organization validates the non-innocent role played by the phenyl-derived PBA side chains. The extent to which structural properties of solubilized porphyrin precursors impact solid-state morphology is further unraveled in Fig. 2b that represents fiber-like materials exclusively constructed from a suspension of supramolecular  $\text{PZn-OAlk-PBA}$  polymer. The entangled aspect indicates that thinner 1D structures assemble by means of hydrophobic interactions to enable the formation of mesoscale, hierarchical fibers such as these observed in Fig. 2b and Fig. S10 (ESI $\ddagger$ ). Considering that the length of a porphyrin building block is 4.5 nm, the recorded height profile of 30 to 60 nm suggests that these fibers are composed of 7 to 15 elementary nanowires. The sharp contrast between the solid-state morphologies of superstructures that derive from individualized  $\text{PZn-OAlk-PBA}$  building blocks and supramolecular polymer derivative underscores the critical role played by precursor conformation in regulating the structure properties of hierarchical materials.

Structure properties of the solid-state composition engendered by aggregation of  $\text{PZn-OAlk-BA}$  building blocks are chronicled in Fig. 2c and d and contrast those elucidated for  $\text{PZn-OAlk-PBA}$  analogs. As evidenced by Fig. 2c and Fig. S12 (ESI $\ddagger$ ), drop-casting  $\text{PZn-OAlk-BA}$  building blocks from parent DMF solution enforces the formation of nanowires. As indicated by a height profile of 3 to 4 nm,  $[\text{PZn-OAlk-BA}]_{\text{NW}}$  nanowires are constructed from one porphyrin building block that stacks along a 1D axis. It is worth noting that this  $\text{PZn-OAlk-BA}$  superstructure conformation differs from that elucidated for  $[\text{PZn-OAlk-PBA}]_{\text{Agg}}$ . The fact that  $\text{PZn-OAlk-BA}$  units form a single-layered superstructure when drop-casted from a DMF solution whereas  $\text{PZn-OAlk-PBA}$  units organize into multi-layered aggregates traces its genesis from the nature of side chains that flank the identical redox active  $\text{PZn-OAlk}$  cores. Confirmed by temperature-dependent aggregation experiments presented earlier,  $\text{PZn-OAlk-BA}$  building blocks form a superstructure in toluene solution with spectral signatures that suggest the existence of J-type aggregates. In agreement with these spectroscopic properties, drop-casted supramolecular  $\text{PZn-OAlk-BA}$  polymer (Fig. 2d) describes a compelling 2D nanostructure by assembling into nanosheets characterized by a height profile of 3 nm. This thickness suggests that 2D nanomaterials created in this manner are composed of a monolayer of interacting porphyrin building blocks. Please note that the seemingly 1D superstructures gleaned in Fig. 2 and Fig. S13 (ESI $\ddagger$ ) are likely to characterize the supramolecular polymer precursors which engender formation of  $\text{PZn-OAlk-BA}$  nanosheets upon drop-casting.

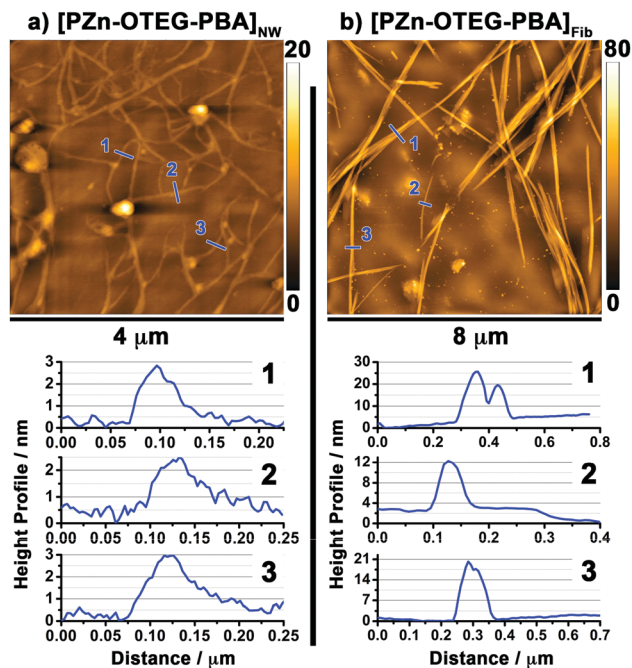


Fig. 3 Topographic intermittent contact mode AFM acquired and associated height profiles recorded for drop-casted: (a)  $[\text{PZn-OTEG-PBA}]_{\text{Agg}}$  aggregates that originate from individualized PZn-derived building blocks in DMF solution; (b)  $[\text{PZn-OTEG-PBA}]_{\text{Fib}}$  fibers constructed from parent PZn-derived supramolecular polymer in toluene solution. For each panel, the height profile corresponds to the associated numbers on the AFM images.

Design principles have been further explored by modulating the amphiphilic character of the PZn core in  $\text{PZn-OTEG-PBA}$  that features hydrophilic ethylene glycol functional groups and identical hydrophobic PBA side chains to those exploited in  $\text{PZn-OAlk-PBA}$ . When compared to  $\text{PZn-OAlk-PBA}$  solid-state structure that features a multi-layered “rod-like” morphology, drop-casted  $\text{PZn-OTEG-PBA}$  building blocks from DMF solution assemble into nanowire superstructures captured in Fig. 3a and Fig. S14 (ESI $\ddagger$ ). The measured thickness of 2.5–3 nm is diagnostic of one porphyrin unit and indicates that  $[\text{PZn-OTEG-PBA}]_{\text{NW}}$  superstructure represents an individualized  $\pi$ -stack. To contrast this observation, supramolecular  $\text{PZn-OTEG-PBA}$  polymer engineered by temperature-dependent aggregation in toluene features rigid-like fibers as presented in Fig. 3b and Fig. S15 (ESI $\ddagger$ ). Similar to the superstructure formed by supramolecular  $\text{PZn-OAlk-PBA}$  polymer,  $[\text{PZn-OTEG-PBA}]_{\text{Fib}}$  self-assemblies consist of several interacting nanowires as attested by the recorded height profile of 10 to 25 nm. It is worth noting that on average,  $[\text{PZn-OTEG-PBA}]_{\text{Fib}}$  superstructures are thinner than  $[\text{PZn-OAlk-PBA}]_{\text{Fib}}$ , the origin of which can be traced from the solubility of respective building blocks.

The formation process of PZn-derived superstructures as a function of solubilized precursors is summarized in Fig. 4. Because temperature-dependent aggregation of supramolecular  $\text{PZn-OAlk-PBA}$  and  $\text{PZn-OTEG-PBA}$  polymers reveals the spectroscopic fingerprints of H-type aggregates, the conformation of the building blocks that construct these  $\pi$ -conjugated superstructures is best described by a co-facial arrangement. During evaporation

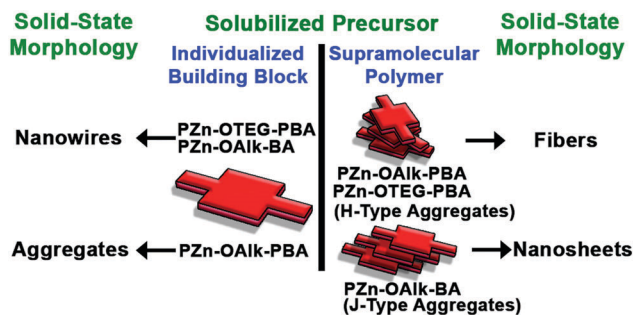


Fig. 4 Summary of the solid-state morphologies delineated by PZn-derived building blocks and supramolecular polymers.

on a solid-state substrate, these two PZn-derived supramolecular polymers evolve into higher-ordered fiber-like materials. In contrast, slipped geometry of J-type aggregate best describes the conformation of building blocks that comprise  $\text{PZn-OAlk-BA}$  supramolecular polymer as suggested by the Kasha model. This aggregate conformation has a drastic impact during the evaporation of supramolecular  $\text{PZn-OAlk-BA}$  polymers as it engenders the formation of 2D nanosheets. Since  $\text{PZn-OAlk-BA}$  and  $\text{PZn-OAlk-PBA}$  share an identical redox active core, the discrepancy of aggregate properties originates solely from the structural properties of the PBA and BA side chains. It is well established that minor structural modification of the peripheral side chains that flank rigid  $\pi$ -conjugated cores can enable drastic changes in material morphologies.<sup>63,64</sup> Furthermore, we hypothesize that the difference of solid-state morphologies observed when comparing  $[\text{PZn-OAlk-PBA}]_{\text{Fib}}$  and  $[\text{PZn-OAlk-PBA}]_{\text{NS}}$  traces its genesis from the strength of the hydrophobic interactions between supramolecular precursors. With respect to a BA side chain that contains one alkyl functional group, a PBA unit features two hydrophobic fragments that describe a triangular shape. In addition to the nature of the aggregate that composes PZn-derived supramolecular polymers, stronger hydrophobic interaction between  $\text{PZn-OAlk-PBA}$  and  $\text{PZn-OTEG-PBA}$  supramolecular polymers when compared to  $\text{PZn-OAlk-BA}$  supramolecular polymer enables the formation of higher-ordered hierarchical materials.

Aiming to provide molecular benchmarks with which to further investigate the impact of side chain properties on final superstructure conformation, model compounds  $\text{PZn-OTEG-Tol}$  and  $\text{PZn-OAlk-Tol}$  represented in Scheme 1 were synthesized (see ESI $\ddagger$ ). Please note that these two molecular platforms lack amide functions and as such no secondary interactions other than hydrophobic interactions are possible. Their solid-state properties are presented in Fig. S16 and S17 (ESI $\ddagger$ ). Regardless of the solvent,  $\text{PZn-OAlk-Tol}$  units exist as individualized building blocks at room temperature and describe “platelets” that are 10 to 15 nm thick after drop-casting. Concomitantly, drop-casted  $\text{PZn-OTEG-Tol}$  building blocks feature a granular morphology where no distinct hierarchical architectures can be evidenced. These findings confirm that in concert with PZn amphiphilic characters, BA and PBA side chains regulate the morphologies of hierarchical superstructures.

To glean more insights into the extent to which solid-state morphologies elucidated for PZn-derived hierarchical materials

impact their electronic properties, potentiometric data was acquired for **PZn-OAlk-PBA**, **PZn-OAlk-BA**, and **PZn-OTEG-PBA** assemblies, and were compared to those of control **PZn-OTEG-Tol** and **PZn-OAlk-Tol** samples. Cyclic voltammetry (CV) measurements have been performed exploiting working electrodes on which PZn-based solution has been drop-casted. To ensure reproducibility, each reported potential corresponds to the average of at least 10 measurements, the most representative cyclic voltammograms being represented in Fig. 5, 7 and Fig. S18–S25 (ESI $\ddagger$ ). For the sake of clarity, Fig. 6 summarizes the redox potentials of the **PZn-OAlk**-derived superstructures. As presented in Fig. 5 and Fig. S24 (ESI $\ddagger$ ), the analysis of CV measurements recorded for **[PZn-OAlk-PBA]<sub>Fib</sub>**, **[PZn-OAlk-PBA]<sub>Agg</sub>**, and **[PZn-OAlk-Tol]<sub>Agg</sub>** indicates a minor perturbation of the oxidation potentials as a function of superstructure conformation. In sharp contrast, the reduction potentials recorded for these three assemblies suggest that superstructure conformations considerably impact the potentials required to inject negative charge carriers into their respective conduction bands. The apparent less negative reduction potential recorded for **[PZn-OAlk-PBA]<sub>Fib</sub>** ( $E^{-/0} = -941$  mV) when compared to control **[PZn-OAlk-Tol]<sub>Agg</sub>** ( $E^{-/0} = -1010$  mV) and **[PZn-OAlk-PBA]<sub>Agg</sub>** ( $E^{-/0} = -1000$  mV) indicates that the fiber-like conformation enforces the formation of a conduction band that is more stabilized than that evidenced in the aggregate derivatives. Such a difference in potentiometric properties underscores the critical role played by supramolecular pathway selection of porphyrin building blocks to modulate structure–function properties of hierarchical materials. As highlighted earlier when discussing self-assembly mechanisms and solid-state properties, fiber-like domains are exclusively formed

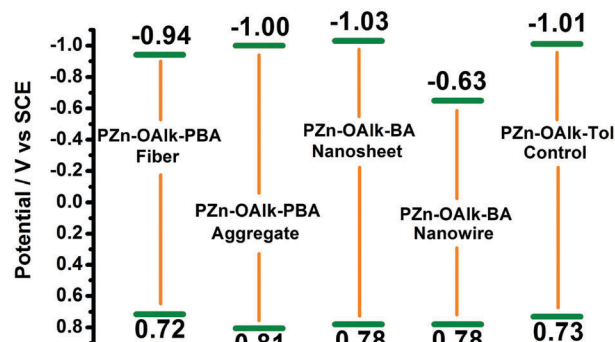


Fig. 6 Diagram that summarizes the recorded oxidation and reduction potentials as a function of **PZn-OAlk**-derived superstructure morphologies.

from solution-based supramolecular polymers that regulate the interaction of porphyrin building blocks whereas nano-aggregates originate from assembly of molecularly dissolved building blocks. The lower potential at which electrons are injected into the conduction band of **[PZn-OAlk-PBA]<sub>Fib</sub>** when compared to that of **[PZn-OAlk-PBA]<sub>Agg</sub>** and **[PZn-OAlk-Tol]<sub>Agg</sub>** suggests a stronger electronic coupling between building blocks and may indicate a higher degree of charge delocalization enforced by the fiber conformation.

Electrochemical measurements performed on **PZn-OAlk-BA** solid-state assemblies differ from that recorded for **PZn-OAlk-PBA** compositions and place further emphasis on the structure–function relationships of supramolecular assemblies. The oxidation and reduction potentials probed for **[PZn-OAlk-BA]<sub>NS</sub>** are chronicled in Fig. 5c ( $E^{0/+} = 780$  mV;  $E^{-/0} = -1030$  mV) and appear more positive

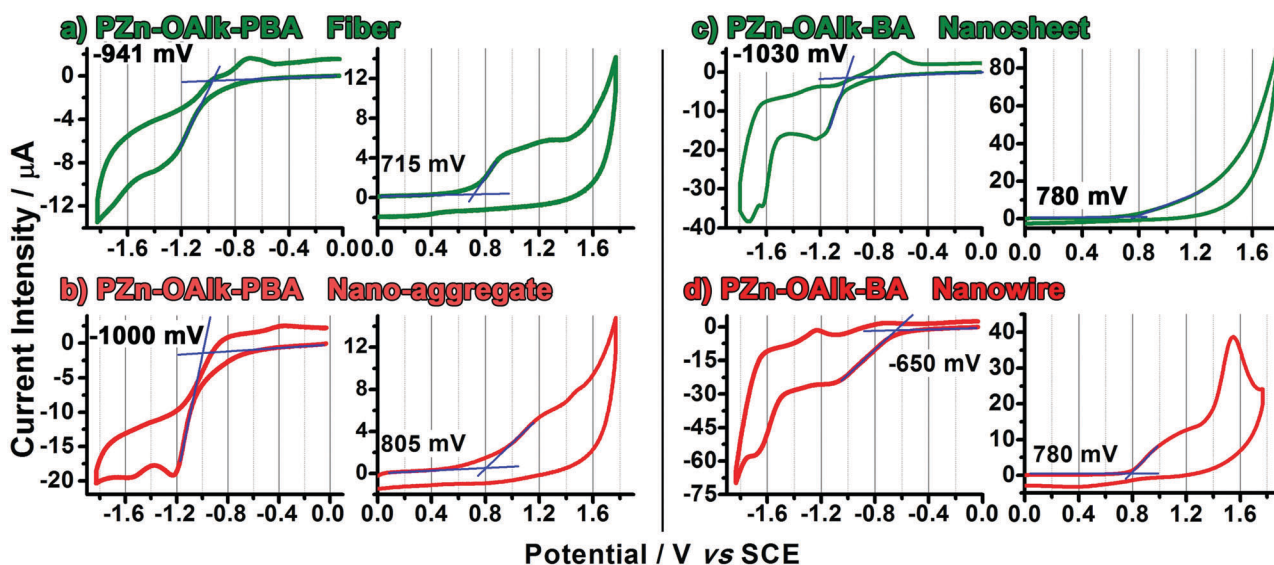


Fig. 5 Cyclic voltammetry measurements that chronicle the anodic and cathodic redox processes of (porphinato)zinc(II) superstructures drop-casted on a glassy carbon working electrode: (a) **PZn-OAlk-PBA** fibers from supramolecular polymer precursors, (b) **PZn-OAlk-PBA** nanoaggregates from individualized building blocks, (c) **PZn-OAlk-BA** nanosheets from supramolecular precursors, and (d) **PZn-OAlk-BA** nanowires from individualized building blocks. The blue lines correspond to the tangents used to measure the onset potentials. All measurements are being reported against sodium calomel electrode (SCE) using  $\text{Fc}/\text{Fc}^+$  as an internal potentiometric standard  $\text{Fc}/\text{Fc}^+ = 0.40$  V vs. SCE in acetonitrile. Experimental conditions: 0.1 M TBAP, scan rate =  $100 \text{ mV s}^{-1}$ , glassy carbon electrode,  $\text{Ag}/\text{AgCl}$  reference electrode. To ensure reproducibility, all the presented measurements have been recorded from different batches. Additional CV measurements are reported in Fig. S18–S21 (ESI $\ddagger$ ).

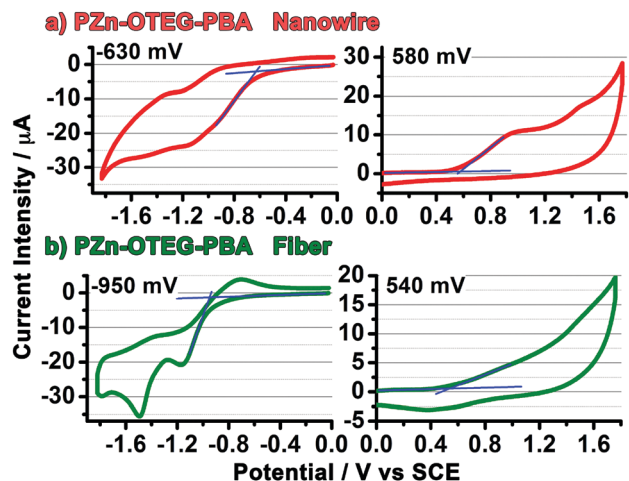


Fig. 7 Cyclic voltammetry measurements that chronicle the anodic and cathodic redox processes of (porphinato)zinc(II) superstructures drop-casted on a glassy carbon working electrode: (a) **PZn-OTEG-PBA** nanowire from individualized building blocks, (b) **PZn-OTEG-PBA** fiber from supramolecular polymer. The blue lines correspond to the tangents used to measure the onset potentials. All measurements are being reported against sodium calomel electrode (SCE) using  $Fc/Fc^+$  as an internal potentiometric standard  $Fc/Fc^+ = 0.40$  V vs. SCE in acetonitrile. Experimental conditions: 0.1 M TBAP, scan rate =  $100$   $\text{mV s}^{-1}$ , glassy carbon electrode, Ag/AgCl reference electrode. To ensure reproducibility, all the presented measurements have been recorded from different batches. Additional CV measurements are reported in Fig. S22 and S23 (ESI $\ddagger$ ).

( $E^{0/+} = +65$  mV) and more negative ( $E^{-/0} = -89$  mV) than that elucidated for  $[PZn-Oalk-PBA]_{Fib}$ . The fact that  $[PZn-Oalk-PBA]_{Fib}$  conformation promotes the formation of valence and conduction bands that are destabilized and stabilized with respect to those formed in  $[PZn-Oalk-BA]_{NS}$  traces its genesis from the properties of the aggregates that comprise these superstructures.

Congruent with the optical properties evidenced by  $[PZn-Oalk-BA]_{NS}$ , J-type aggregates best describe this self-assembled superstructure and suggest a lesser degree of frontier molecular orbital (FMO) overlap when compared to H-type aggregates that construct  $[PZn-Oalk-PBA]_{Fib}$ .<sup>24–26</sup> Consequently, lower potentials are required to inject charges into fiber-like superstructure with a conformation that promotes stronger electronic coupling between repeating units. This assumption is further confirmed when comparing the potentiometric properties of  $[PZn-Oalk-BA]_{NW}$  and  $[PZn-Oalk-BA]_{NS}$  presented in Fig. 5c and d. Nanowires formed by drop-casting a DMF solution of **PZn-Oalk-BA** building blocks manifest a reduction potential ( $E^{-/0} = -650$  mV) less negative by more than 350 mV when compared to  $[PZn-Oalk-BA]_{NS}$ . The apparent stabilization of the conduction band energy observed in  $[PZn-Oalk-BA]_{NW}$  points toward the non-innocent role played by the aggregate properties. Building block conformation in a J-type aggregate is best described by a slipped geometry that while enforcing coupling of the transition dipole moment, reduces FMO overlaps. In contrast, cofacial geometry that describes conformation of H-type aggregates can enforce stronger interaction of the FMO between adjacent building blocks and may favour a higher degree of charge delocalization. Because only a minor perturbation of the valence band energies can be gleaned when

comparing the electronic structures of nanosheets, fibers, and nanowire superstructures, we postulate that these self-assembly conformations do not perturb the interaction of PZn HOMO with a magnitude that can be detected by CV measurements. In contrast, the fact that a less negative potential can be utilized to inject electrons into the conduction band of **PZn-Oalk-BA** nanowires with respect to that of **PZn-Oalk-BA** nanosheets may be diagnostic of a larger degree of electronic coupling between the PZn LUMOs in 1D assemblies than in 2D superstructures.

It is also worth noting the drastic difference of reduction potential when comparing  $[PZn-Oalk-BA]_{NW}$  ( $E^{-/0} = -650$  mV) and  $[PZn-Oalk-PBA]_{Fib}$  ( $E^{-/0} = -965$  mV). Because **PZn-Oalk**-derived fiber and nanowire superstructures share identical redox active PZn subunits and comparable solid-state morphologies (both are 1D materials), the evident discrepancy when comparing the potentiometric properties of these two self-assemblies cannot be solely attributed to a perturbation of porphyrin–porphyrin electronic interaction. Rather, we believe that the more negative potential required to inject electrons into the  $[PZn-Oalk-PBA]_{Fib}$  conduction band when compared to  $[PZn-Oalk-BA]_{NW}$  may trace its genesis from a screening effect. As evidenced by AFM investigation, fibers built from **PZn-Oalk-PBA** building blocks feature a thickness ranging from 30 nm to 60 nm. Considering that the length of one PZn repeating unit is 4.5 nm, these fibers are composed of 7 to 14 entangled nanowires. Consequently, initially injected electrons at less negative potentials may screen the injection of additional charges therefore imposing the use of a more negative potential to fully reduce the entire superstructure. Please note that the screening effect in multi-layered semiconducting materials is a well-established electronic phenomenon that notoriously perturbs investigation of charge transport properties in field-effect transistors.<sup>65–67</sup>

Potentiometric data recorded for **PZn-OTEG-PBA** superstructures are presented in Fig. 7 and confirm initial structure–function relationships elucidated for **PZn-Oalk**-derived hierarchical materials. To facilitate the discussion, all redox potentials recorded for **PZn-OTEG**-derived superstructures are summarized in Fig. 8. When compared to electrochemical measurements performed on **PZn-OTEG-Tol** control sample (Fig. S25, ESI $\ddagger$ ;  $E^{0/+} = 600$  mV;  $E^{-/0} = -1000$  mV), lower cathodic ( $E^{-/0} = -950$  mV) and anodic potentials ( $E^{0/+} = 540$  mV) are necessary to inject electrons and holes into the conduction and valence bands of  $[PZn-OTEG-PBA]_{Fib}$  superstructures. Furthermore, the fact that the elementary nanowires that construct  $[PZn-OTEG-PBA]_{Fib}$  superstructures can be formed by drop-casting individualized **PZn-OTEG-PBA** building blocks from a DMF solution provides samples with which to unambiguously probe the potentiometric properties of a fundamental  $\pi$ -stack. Mimicking the structure–function properties unveiled for **PZn-Oalk**-derived nanowires and fibers, potentiometric data recorded for  $[PZn-OTEG-PBA]_{NW}$  underscore a drastic decrease of the reduction potential ( $E^{0/+} = -630$  mV) when compared to  $[PZn-OTEG-PBA]_{Fib}$  ( $E^{0/+} = -950$  mV) while only a minor perturbation of the oxidation potentials can be appreciated. The apparent less negative potential required to inject negative charge carriers into  $[PZn-OTEG-PBA]_{NW}$  conduction band when

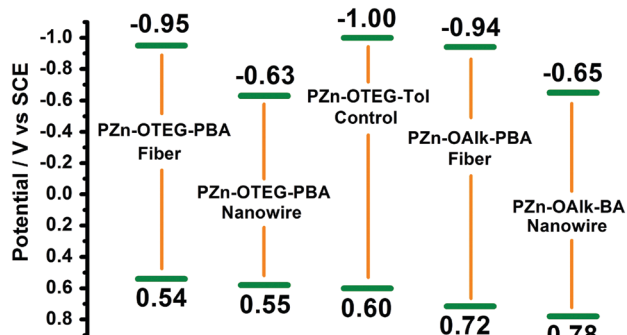


Fig. 8 Diagram that compares the recorded oxidation and reduction potentials as a function of PZn-OATEG-derived and relevant PZn-OAlk-relevant superstructure morphologies.

compared to [PZn-OATEG-PBA]<sub>Fib</sub> supports our initial hypothesis that: (1) screening effect in higher-order hierarchical materials may plague the accurate assessment of the potentiometric properties that characterize elementary constituent, and (2) electrochemical measurements exclusively performed on elementary nanowire can provide reliable potentials with which to assess valence and conduction band energies of fundamental  $\pi$ -stacks (Fig. 8).

In addition, comparing the oxidation and reduction potentials recorded for [PZn-OATEG-Tol]<sub>Agg</sub> and [PZn-OATEG-PBA]<sub>NW</sub> provides important insight onto the structure–function properties of  $\pi$ -conjugated superstructures. Relative to [PZn-OATEG-Tol]<sub>Agg</sub>, the apparent less negative potential ( $E^{+/0} = -630$  mV) required to inject negative charge carriers into the conduction band of [PZn-OATEG-PBA]<sub>NW</sub> indicates a superstructure conformation that enforces stronger electronic coupling between porphyrin repeating units. The fact that only a minor perturbation of the oxidation potential can be detected across [PZn-OATEG-PBA]<sub>NW</sub>, [PZn-OATEG-PBA]<sub>Fib</sub>, and [PZn-OATEG-PBA]<sub>Agg</sub> suggests that superstructure conformation plays a minor role in mixing the HOMO energy level of porphyrin repeating units but, in contrast, enforces a non-negligible interaction between the LUMO energy level of PZn building blocks the magnitude of which can be detected by CV measurements.

## Conclusions

In summary, we have reported the synthesis, characterization and self-assembly properties of novel (porphinato)zinc(II) building blocks. Modification of the side chain structures that flank PZn-redox active cores enables controlling the conformation of hierarchical materials with structure–function relationships that have been unveiled for the first time by cyclic voltammetry experiments. As evidenced by a systematic AFM investigation, while solubilized PZn-OATEG-PBA and PZn-OAlk-BA building blocks form 1D nanowires through drop-casting deposition, their respective solution-based supramolecular polymer precursors provide formation of fiber-like materials and 2D nanosheets in the solid state. The evidenced discrepancy when monitoring superstructure morphologies underscores the cardinal role played not only by processing conditions but also by the structural properties

of parent solubilized precursors. The panoply of superstructure conformation has allowed us to systematically investigate the potentiometric data of these hierarchical semiconducting materials and establish the energy level of the conduction and valence bands with respect to the SCE reference electrode.

A general trend emerges: while superstructure conformation modestly perturbs the energies of valence bands across the PZn-OATEG and PZn-OAlk series, a drastic change of conduction band energies can be deciphered. For identical redox-active cores and comparable superstructure morphologies, the less negative potential required to reduce PZn-derived nanowires when compared to PZn-derived fibers indicates that the electronic properties of the fundamental  $\pi$ -stacks constructing higher ordered hierarchical objects can exclusively be assessed when probing nanowires at the individualized levels. Furthermore, the fact that 2D PZn-OAlk-BA nanosheets built from a single-layer of interacting (porphinato)zinc(II) units evidences a reduction potential destabilized by more than 350 mV when compared to that of PZn-OAlk-BA nanowires may differentiate the role played by J- and H-type aggregates in dictating the potentiometric properties of final superstructures. Because this work demonstrates that electronic properties of  $\pi$ -conjugated supramolecular polymers and related superstructures can be probed using conventional cyclic voltammetry experiments, we posit that electrochemical methods will expand the tool box to scrutinize structure–function relationships of self-assembled hierarchical materials and will shed new light on their electronic properties.

## Experimental

### Materials and instrumentation

All water-sensitive and oxygen-sensitive compounds were stored and handled in a Braun Labmaster DP glovebox. Standard Schlenk techniques were employed to manipulate water-sensitive and oxygen-sensitive reactions. Only ultrapure argon purchased from Airgas was used. All deuterated solvents were purchased from Cambridge Isotope Laboratories, Inc. Methanol, ethanol, hexane, acetone, chloroform, dichloromethane, toluene, *N,N*-dimethylformamide (DMF), tetrahydrofuran (THF), sodium chloride and silica gel (70–90  $\mu$ m) were purchased from VWR International. All distilled THF was prepared under argon from a sodium/benzophenone distillation device. Sodium sulfate, sodium chloride, potassium carbonate, diisopropylamine, tetrabutylammonium fluoride (1 M solution in THF) and tetrabutylammonium hexafluorophosphate were purchased from Sigma-Aldrich. Copper(I) iodide, sodium, benzophenone, (triisopropylsilyl)acetylene and propargylamine were purchased from Alfa Aesar. Dodecanoyl chloride, 1,4-dibromobenzene, *N,N*-dimethylpyridin-4-amine and *N*-(3-dimethylaminopropyl)-*N'*-ethylcarbodiimide hydrochloride were purchased from Tokyo Chemical Industry Co., Ltd. Tetrakis-(triphenylphosphine)palladium(0) was purchased from Strem Chemicals. Size exclusion chromatography was performed using Bio-Beads S-X1 Support purchased from Bio-Rad Laboratories, Inc. Nuclear magnetic resonance (NMR) spectroscopy was performed

on a Bruker Avance 400 MHz NMR spectrometer. Ultraviolet-visible (UV-Vis) spectrophotometry was performed on a Cary 5000 UV-Vis-NIR spectrophotometer. Fourier-transform infrared (FTIR) spectroscopy was performed on a PerkinElmer Frontier FTIR spectrometer. Cyclic voltammetry (CV) was performed on a PARSTAT 3000A potentiostat/galvanostat/EIS analyzer. Electro-spray ionization mass spectrometry (ESI-MS) was performed on a Bruker MicroQ-TOF III ESI mass spectrometer. Matrix-assisted laser desorption/ionization mass spectrometry (MALDI-MS) was performed on a Bruker Autoflex III MALDI mass spectrometer. Atomic force microscopy (AFM) was performed on an Agilent 5420 AFM/SPM microscope. Silicon wafers (0.5 mm) used to prepare AFM samples were purchased from UniversityWafer, Inc.

### AFM sample preparation

Silicon wafers were soaked in ethanol for 1 h and washed with acetone. Porphyrin solutions that had undergone corresponding temperature ramping UV-Vis experiments were drop-casted onto the wafers. When no solvent droplets were visible, the wafers were dried under vacuum.

### CV measurements

A glassy carbon working electrode, a platinum counter electrode and a Ag/AgCl (3 M NaCl) reference electrode were used. The ferrocene/ferrocenium redox couple was used as an internal potentiometric standard. Measurements were performed using tetrabutylammonium hexafluorophosphate (0.1 M) as the electrolyte in distilled acetonitrile under argon. Porphyrin solutions that had undergone corresponding temperature ramping UV-Vis experiments were drop-casted onto the electrode ( $7 \times 50 \mu\text{L}$ ) and dried under vacuum. For each sample, cathodic and anodic cycles ( $0.1 \text{ V s}^{-1}$  for both) were scanned separately, and each cycle was repeated for three times with the average oxidation/reduction potentials taken. Upon determination of the oxidation/reduction potentials, the onset points were taken where the current started to deviate from the baseline.

**(5,15-Bis[2-[3,5-bis(dodecanoylamino)-4-methylphenyl]ethynyl]-10,20-bis[2-(3,5,5-trimethylhexyloxy)ethyl]porphinato)zinc(II) PZn-Oalk-PBA.** The synthetic pathway is presented in Scheme S5 (ESI $\ddagger$ ). {5,15-Dibromo-10,20-bis[2-(3,5,5-trimethylhexyloxy)ethyl]porphinato}zinc(II) (**18**) ( $0.100 \text{ g}$ ,  $1.15 \times 10^{-4} \text{ mol}$ ), *N,N'*-(5-ethynyl-2-methyl-1,3-phenylene)dodecanamide (**12**) ( $0.200 \text{ g}$ ,  $3.92 \times 10^{-4} \text{ mol}$ ), CuI ( $2.20 \text{ mg}$ ,  $1.16 \times 10^{-5} \text{ mol}$ ) and Pd(PPh $_3$ ) $_4$  ( $20.0 \text{ mg}$ ,  $1.73 \times 10^{-5} \text{ mol}$ ) were added into a Schlenk flask in a glove box. After 60 mL of distilled THF and 15 mL of dry (Me $_2$ CH) $_2$ NH were mixed, freeze-pump-thawed and cannulated into the Schlenk flask, the reaction mixture was stirred at 60 °C for 12 h under Ar. After solvent removal, the solid was dispersed in 100 mL of THF, and the mixture was refluxed for 30 min and filtered. The above operation was repeated for seven times (a Soxhlet extractor can be used as well for better efficiency). All filtrate was combined and the solvent was evaporated. The resulting solid was dispersed in the mixture of 40 mL of CH $_3$ OH and 40 mL of THF, and the mixture was refluxed for 30 min and cooled to room temperature. After filtration, the collected solid was dried under vacuum to give the desired product as a green

solid ( $0.041 \text{ g}$ , 21%).  $^1\text{H NMR}$  (400 MHz, THF-D $_8$  with two drops of CDCl $_3$  and one drop of pyridine-D $_5$ , 333 K)  $\delta = 9.70$  (d, 4H,  $J = 4.0 \text{ Hz}$ ), 9.47 (d, 4H,  $J = 4.4 \text{ Hz}$ ), 8.24 (br, 4H), 8.04 (s, 4H), 5.15 (t, 4H,  $J = 8.0 \text{ Hz}$ ), 4.39 (t, 4H,  $J = 7.4 \text{ Hz}$ ), 3.55 (t, 4H,  $J = 6.0 \text{ Hz}$ ), 2.45 (t, 8H,  $J = 7.2 \text{ Hz}$ ), 2.24 (s, 6H), 2.2–1.0 (m, 82H), 1.0–0.8 (m, 36H) ppm. MALDI-MS  $m/z$ : 1730.04 ( $[\text{M} + \text{H}]^+$ , calcd for 1730.18). Note: because of the low solubility of this compound, there were not enough signals when  $^{13}\text{C NMR}$  was performed.

**(5,15-Bis[2-[4-(4,8-diaza-5,9-dioxoicosynyl)phenyl]ethynyl]-10,20-bis[2-(3,5,5-trimethylhexyloxy)ethyl]porphinato)zinc(II) PZn-Oalk-BA.** The synthetic pathway is presented in Scheme S4 (ESI $\ddagger$ ). {5,15-Dibromo-10,20-bis[2-(3,5,5-trimethylhexyloxy)ethyl]porphinato}zinc(II) (**18**, Scheme S4, ESI $\ddagger$ ) ( $0.0750 \text{ g}$ ,  $8.60 \times 10^{-5} \text{ mol}$ ), 4-aza-*N*-[3-(4-ethynylphenyl)prop-2-ynyl]-5-oxododecanamide (**7**, Scheme S4, ESI $\ddagger$ ) ( $0.110 \text{ g}$ ,  $2.69 \times 10^{-4} \text{ mol}$ ), CuI ( $1.10 \text{ mg}$ ,  $5.78 \times 10^{-6} \text{ mol}$ ) and Pd(PPh $_3$ ) $_4$  ( $7.00 \text{ mg}$ ,  $6.06 \times 10^{-6} \text{ mol}$ ) were added into a Schlenk flask in a glove box. After 50 mL of distilled THF and 10 mL of dry (Me $_2$ CH) $_2$ NH were mixed, freeze-pump-thawed and cannulated into the Schlenk flask, the reaction mixture was stirred at 60 °C for 12 h under Ar and passed through a silica plug using THF as the eluent. After solvent removal, the residue was chromatographed first on silica using 20:1 CHCl $_3$ :CH $_3$ OH as the eluent and then on a size exclusion column using THF as the eluent. The collected solid was washed with CH $_3$ OH and dried under vacuum to give the desired product as a green solid ( $0.020 \text{ g}$ , 15%).  $^1\text{H NMR}$  (400 MHz, CDCl $_3$  with a drop of pyridine-D $_5$ )  $\delta = 9.69$  (d, 4H,  $J = 4.4 \text{ Hz}$ ), 9.47 (d, 4H,  $J = 4.8 \text{ Hz}$ ), 7.96 (d, 4H,  $J = 8.0 \text{ Hz}$ ), 7.61 (d, 4H,  $J = 8.4 \text{ Hz}$ ), 6.31 (br, 2H), 6.25 (br, 2H), 5.17 (t, 4H,  $J = 7.4 \text{ Hz}$ ), 4.41 (t, 4H,  $J = 7.6 \text{ Hz}$ ), 4.38 (d, 4H,  $J = 5.2 \text{ Hz}$ ), 3.60 (q, 4H,  $J = 6.4 \text{ Hz}$ ), 3.59 (t, 4H,  $J = 6.4 \text{ Hz}$ ), 2.53 (t, 4H,  $J = 6.2 \text{ Hz}$ ), 2.19 (t, 4H,  $J = 7.8 \text{ Hz}$ ), 2.0–1.0 (m, 46H), 1.0–0.8 (m, 30H) ppm.  $^{13}\text{C NMR}$  (101 MHz, CDCl $_3$  with a drop of pyridine-D $_5$ )  $\delta = 173.6$ , 171.4, 151.2, 150.4, 132.0, 131.3, 131.1, 129.4, 124.6, 122.1, 117.6, 99.7, 95.7, 95.5, 86.6, 83.4, 77.2, 69.7, 51.2, 39.2, 36.9, 35.9, 35.6, 35.3, 31.9, 31.1, 30.1, 30.0, 29.6, 29.6, 29.5, 29.4, 29.3, 29.3, 26.2, 25.8, 22.8, 22.7, 14.1 ppm. MALDI-MS  $m/z$ : 1526.82 ( $[\text{M} + \text{H}]^+$ , calcd for 1526.91).

**[5,15-Bis[2-[3,5-bis(dodecanoylamino)-4-methylphenyl]ethynyl]-10,20-bis(3,5-bis[2-[2-(2-methoxyethoxy)ethoxy]ethoxy]phenyl)porphinato]zinc(II) PZn-OTEG-PBA.** The synthetic pathway is presented in Scheme S7 (ESI $\ddagger$ ). [5,15-Bis(3,5-bis[2-[2-(2-methoxyethoxy)ethoxy]ethoxy]phenyl)-10,20-dibromoporphinato]zinc(II) (**23**) ( $0.0900 \text{ g}$ ,  $6.75 \times 10^{-5} \text{ mol}$ ), *N,N'*-(5-ethynyl-2-methyl-1,3-phenylene)dodecanamide (**12**) ( $0.104 \text{ g}$ ,  $2.04 \times 10^{-4} \text{ mol}$ ), CuI ( $1.30 \text{ mg}$ ,  $6.83 \times 10^{-6} \text{ mol}$ ) and Pd(PPh $_3$ ) $_4$  ( $11.0 \text{ mg}$ ,  $9.52 \times 10^{-6} \text{ mol}$ ) were added into a Schlenk flask in a glove box. After 50 mL of distilled THF and 10 mL of dry (Me $_2$ CH) $_2$ NH were mixed, freeze-pump-thawed and cannulated into the Schlenk flask, the reaction mixture was stirred at 60 °C for 12 h under Ar and passed through a silica plug using THF as the eluent. After solvent removal, the residue was chromatographed first on silica using 10:1 CHCl $_3$ :CH $_3$ OH as the eluent and then on a size exclusion column using THF as the eluent. The collected solid was washed with CH $_3$ OH and dried under vacuum to give the desired product as a green solid ( $0.057 \text{ g}$ , 39%).  $^1\text{H NMR}$  (400 MHz, CDCl $_3$  with a drop of pyridine-D $_5$ )  $\delta = 9.64$

(d, 4H,  $J = 4.4$  Hz), 8.90 (d, 4H,  $J = 4.8$  Hz), 8.07 (br, 4H), 7.43 (br, 4H), 7.37 (d, 4H,  $J = 2.0$  Hz), 6.95 (t, 2H,  $J = 2.0$  Hz), 4.33 (t, 8H,  $J = 4.8$  Hz), 3.96 (t, 8H,  $J = 4.8$  Hz), 3.79 (m, 8H), 3.71 (m, 8H), 3.64 (m, 8H), 3.50 (m, 8H), 3.32 (s, 12H), 2.49 (t, 8H,  $J = 6.8$  Hz), 2.24 (s, 6H), 2.0–1.0 (m, 72H), 0.87 (t, 12H,  $J = 5.8$  Hz) ppm.  $^{13}\text{C}$  NMR (101 MHz,  $\text{CDCl}_3$  with a drop of pyridine- $\text{D}_5$ )  $\delta = 172.1, 157.8, 151.8, 149.5, 144.5, 136.5, 132.3, 130.7, 127.3, 125.6, 124.6, 122.5, 121.9, 114.9, 101.0, 95.5, 93.6, 71.9, 70.9, 70.7, 70.5, 69.9, 67.8, 59.0, 37.2, 31.9, 29.6, 29.6, 29.6, 29.5, 29.4, 29.3, 29.3, 25.8, 22.6, 14.1$  ppm. MALDI-MS  $m/z$ : 2191.27 ( $[\text{M} + \text{H}]^+$ , calcd for 2191.27).

## Conflicts of interest

There are no conflicts to declare.

## Acknowledgements

This work was made possible by The University of Miami Startup Fund. The authors thank Prof. Roger Leblanc for his assistance with atomic force microscopy.

## Notes and references

- 1 T. Hasobe, K. Saito, P. V. Kamat, V. Troiani, H. Qiu, N. Solladie, K. S. Kim, J. K. Park, D. Kim, F. D'Souza and S. Fukuzumi, Organic solar cells. Supramolecular composites of porphyrins and fullerenes organized by polypeptide structures as light harvesters, *J. Mater. Chem.*, 2007, **17**, 4160–4170.
- 2 V. V. Roznyatovskiy, R. Carmieli, S. M. Dyar, K. E. Brown and M. R. Wasielewski, Photodriven Charge Separation and Transport in Self-Assembled Zinc Tetrabenzotetraphenylporphyrin and Perylenediimide Charge Conduits, *Angew. Chem., Int. Ed.*, 2014, **53**, 3457–3461.
- 3 P.-O. Schwartz, L. Biniak, E. Zaborova, B. Heinrich, M. Brinkmann, N. Leclerc and S. Méry, Perylenediimide-Based Donor–Acceptor Dyads and Triads: Impact of Molecular Architecture on Self-Assembling Properties, *J. Am. Chem. Soc.*, 2014, **136**, 5981–5992.
- 4 N. J. Hestand, R. V. Kazantsev, A. S. Weingarten, L. C. Palmer, S. I. Stupp and F. C. Spano, Extended-Charge-Transfer Excitons in Crystalline Supramolecular Photocatalytic Scaffolds, *J. Am. Chem. Soc.*, 2016, **138**, 11762–11774.
- 5 A. T. Haedler, K. Kreger, A. Issac, B. Wittmann, M. Kivala, N. Hammer, J. Köhler, H.-W. Schmidt and R. Hildner, Long-range energy transport in single supramolecular nanofibres at room temperature, *Nature*, 2015, **523**, 196.
- 6 L. F. Dössel, V. Kamm, I. A. Howard, F. Laquai, W. Pisula, X. Feng, C. Li, M. Takase, T. Kudernac, S. De Feyter and K. Müllen, Synthesis and Controlled Self-Assembly of Covalently Linked Hexa-peri-hexabenzocoronene/Perylene Diimide Dyads as Models To Study Fundamental Energy and Electron Transfer Processes, *J. Am. Chem. Soc.*, 2012, **134**, 5876–5886.
- 7 J. H. Olivier, J. Park, P. Deria, J. Rawson, Y. Bai, S. Kumbhar Amar and J. Therien Michael, Unambiguous Diagnosis of Photoinduced Charge Carrier Signatures in a Stoichiometrically Controlled Semiconducting Polymer-Wrapped Carbon Nanotube Assembly, *Angew. Chem., Int. Ed.*, 2015, **54**, 8133–8138.
- 8 P. Gawrys, D. Boudinet, A. Kornet, D. Djurado, S. Pouget, J.-M. Verilhac, M. Zagorska and A. Pron, Organic semiconductors for field-effect transistors (FETs): tuning of spectroscopic, electrochemical, electronic and structural properties of naphthalene bisimides via substituents containing alkylthienyl moieties, *J. Mater. Chem.*, 2010, **20**, 1913–1920.
- 9 H. Ma, N. Liu and J.-D. Huang, A DFT Study on the Electronic Structures and Conducting Properties of Rubrene and its Derivatives in Organic Field-Effect Transistors, *Sci. Rep.*, 2017, **7**, 331.
- 10 K. Xiao, Y. Liu, T. Qi, W. Zhang, F. Wang, J. Gao, W. Qiu, Y. Ma, G. Cui, S. Chen, X. Zhan, G. Yu, J. Qin, W. Hu and D. Zhu, A Highly  $\pi$ -Stacked Organic Semiconductor for Field-Effect Transistors Based on Linearly Condensed Pentathienoacene, *J. Am. Chem. Soc.*, 2005, **127**, 13281–13286.
- 11 V. Coropceanu, J. Cornil, D. A. da Silva Filho, Y. Olivier, R. Silbey and J.-L. Brédas, Charge Transport in Organic Semiconductors, *Chem. Rev.*, 2007, **107**, 926–952.
- 12 M. Mas-Torrent and C. Rovira, Role of Molecular Order and Solid-State Structure in Organic Field-Effect Transistors, *Chem. Rev.*, 2011, **111**, 4833–4856.
- 13 S. Pramanik, C. G. Stefanita, S. Patibandla, S. Bandyopadhyay, K. Garre, N. Harth and M. Cahay, Observation of extremely long spin relaxation times in an organic nanowire spin valve, *Nat. Nanotechnol.*, 2007, **2**, 216.
- 14 K. Michaeli, N. Kantor-Uriel, R. Naaman and D. H. Waldeck, The electron's spin and molecular chirality – how are they related and how do they affect life processes?, *Chem. Soc. Rev.*, 2016, **45**, 6478–6487.
- 15 W. Mtangi, F. Tassinari, K. Vankayala, A. Vargas Jentzsch, B. Adelizzi, A. R. A. Palmans, C. Fontanesi, E. W. Meijer and R. Naaman, Control of Electrons' Spin Eliminates Hydrogen Peroxide Formation During Water Splitting, *J. Am. Chem. Soc.*, 2017, **139**, 2794–2798.
- 16 V. Kiran, P. Mathew Shinto, R. Cohen Sidney, I. Hernández Delgado, J. Lacour and R. Naaman, Helicenes—A New Class of Organic Spin Filter, *Adv. Mater.*, 2016, **28**, 1957–1962.
- 17 K. E. Martin, Z. Wang, T. Busani, R. M. Garcia, Z. Chen, Y. Jiang, Y. Song, J. L. Jacobsen, T. T. Vu, N. E. Schore, B. S. Swartzentruber, C. J. Medforth and J. A. Shelnutt, Donor–Acceptor Biomorphs from the Ionic Self-Assembly of Porphyrins, *J. Am. Chem. Soc.*, 2010, **132**, 8194–8201.
- 18 J.-L. Brédas, J. E. Norton, J. Cornil and V. Coropceanu, Molecular Understanding of Organic Solar Cells: The Challenges, *Acc. Chem. Res.*, 2009, **42**, 1691–1699.
- 19 E. Moulin, J.-J. Cid and N. Giuseppone, Advances in Supramolecular Electronics – From Randomly Self-assembled Nanostructures to Addressable Self-Organized Interconnects, *Adv. Mater.*, 2013, **25**, 477–487.
- 20 A. K. Thazhathveetil, M. A. Harris, R. M. Young, M. R. Wasielewski and F. D. Lewis, Efficient Charge Transport

- via DNA G-Quadruplexes, *J. Am. Chem. Soc.*, 2017, **139**, 1730–1733.
- 21 M. Kastler, W. Pisula, F. Laquai, A. Kumar, R. J. Davies, S. Baluschev, M. C. Garcia-Gutiérrez, D. Wasserfallen, H. J. Butt, C. Riekel, G. Wegner and K. Müllen, Organization of Charge-Carrier Pathways for Organic Electronics, *Adv. Mater.*, 2006, **18**, 2255–2259.
  - 22 K. Liu, A. Levy, C. Liu and J.-H. Olivier, Tuning Structure–Function Properties of  $\pi$ -Conjugated Superstructures by Redox-Assisted Self-Assembly, *Chem. Mater.*, 2018, **30**, 2143–2150.
  - 23 O. Ostroverkhova, Organic Optoelectronic Materials: Mechanisms and Applications, *Chem. Rev.*, 2016, **116**, 13279–13412.
  - 24 F. C. Spano and C. Silva, H- and J-Aggregate Behavior in Polymeric Semiconductors, *Annu. Rev. Phys. Chem.*, 2014, **65**, 477–500.
  - 25 N. J. Hestand and F. C. Spano, Molecular Aggregate Photo-physics beyond the Kasha Model: Novel Design Principles for Organic Materials, *Acc. Chem. Res.*, 2017, **50**, 341–350.
  - 26 N. J. Hestand and F. C. Spano, Expanded Theory of H- and J-Molecular Aggregates: The Effects of Vibronic Coupling and Intermolecular Charge Transfer, *Chem. Rev.*, 2018, **118**, 7069–7163.
  - 27 J. Vura-Weis, M. A. Ratner and M. R. Wasielewski, Geometry and Electronic Coupling in Perylenediimide Stacks: Mapping Structure–Charge Transport Relationships, *J. Am. Chem. Soc.*, 2010, **132**, 1738–1739.
  - 28 *Supramolecular Materials for Opto-Electronics*, ed. N. Kock, Royal Chemical Society, 2014, pp. P001–P369.
  - 29 G. Fernández, M. Stolte, V. Stepanenko and F. Würthner, Cooperative Supramolecular Polymerization: Comparison of Different Models Applied on the Self-Assembly of Bis-(merocyanine) Dyes, *Chem. – Eur. J.*, 2012, **19**, 206–217.
  - 30 M. M. J. Smulders, A. P. H. J. Schenning and E. W. Meijer, Insight into the Mechanisms of Cooperative Self-Assembly: The “Sergeants-and-Soldiers” Principle of Chiral and Achiral C3-Symmetrical Discotic Triamides, *J. Am. Chem. Soc.*, 2008, **130**, 606–611.
  - 31 D. Zhao and J. S. Moore, Nucleation–elongation: a mechanism for cooperative supramolecular polymerization, *Org. Biomol. Chem.*, 2003, **1**, 3471–3491.
  - 32 F. Tantakitti, J. Boekhoven, X. Wang, R. V. Kazantsev, T. Yu, J. Li, E. Zhuang, R. Zandi, J. H. Ortony, C. J. Newcomb, L. C. Palmer, G. S. Shekhawat, M. O. de la Cruz, G. C. Schatz and S. I. Stupp, Energy landscapes and functions of supramolecular systems, *Nat. Mater.*, 2016, **15**, 469.
  - 33 M. J. Smulders Maarten, M. L. Nieuwenhuizen Marko, F. A. de Greef Tom, P. van der Schoot, P. H. J. Schenning Albertus and E. W. Meijer, How to Distinguish Isodesmic from Cooperative Supramolecular Polymerisation, *Chem. – Eur. J.*, 2009, **16**, 362–367.
  - 34 S. Ogi, K. Sugiyasu, S. Manna, S. Samitsu and M. Takeuchi, Living supramolecular polymerization realized through a biomimetic approach, *Nat. Chem.*, 2014, **6**, 188.
  - 35 T. Fukui, M. Takeuchi and K. Sugiyasu, Autocatalytic Time-Dependent Evolution of Metastable Two-Component Supramolecular Assemblies to Self-Sorted or Coassembled State, *Sci. Rep.*, 2017, **7**, 2425.
  - 36 T. Fukui, S. Kawai, S. Fujinuma, Y. Matsushita, T. Yasuda, T. Sakurai, S. Seki, M. Takeuchi and K. Sugiyasu, Control over differentiation of a metastable supramolecular assembly in one and two dimensions, *Nat. Chem.*, 2016, **9**, 493.
  - 37 S. Ogi, C. Grzeszkiewicz and F. Würthner, Pathway complexity in the self-assembly of a zinc chlorin model system of natural bacteriochlorophyll J-aggregates, *Chem. Sci.*, 2018, **9**, 2768–2773.
  - 38 R. van der Weegen, J. P. Teunissen Abraham and E. W. Meijer, Directing the Self-Assembly Behaviour of Porphyrin-Based Supramolecular Systems, *Chem. – Eur. J.*, 2017, **23**, 3773–3783.
  - 39 W. Wagner, M. Wehner, V. Stepanenko, S. Ogi and F. Würthner, Living Supramolecular Polymerization of a Perylene Bisimide Dye into Fluorescent J-Aggregates, *Angew. Chem., Int. Ed.*, 2017, **56**, 16008–16012.
  - 40 S. Ogi, V. Stepanenko, K. Sugiyasu, M. Takeuchi and F. Würthner, Mechanism of Self-Assembly Process and Seeded Supramolecular Polymerization of Perylene Bisimide Organogelator, *J. Am. Chem. Soc.*, 2015, **137**, 3300–3307.
  - 41 Z. Xie, B. Xiao, Z. He, W. Zhang, X. Wu, H. Wu, F. Würthner, C. Wang, F. Xie, L. Liu, Y. Ma, W.-Y. Wong and Y. Cao, Self-assembled perylene bisimide J-aggregates as promising cathode modifiers for highly efficient inverted polymer solar cells, *Mater. Horiz.*, 2015, **2**, 514–518.
  - 42 J. Gershberg, F. Fennel, T. H. Rehm, S. Lochbrunner and F. Würthner, Anti-cooperative supramolecular polymerization: a new K2-K model applied to the self-assembly of perylene bisimide dye proceeding *via* well-defined hydrogen-bonded dimers, *Chem. Sci.*, 2016, **7**, 1729–1737.
  - 43 F. Würthner, C. R. Saha-Möller, B. Fimmel, S. Ogi, P. Leowanawat and D. Schmidt, Perylene Bisimide Dye Assemblies as Archetype Functional Supramolecular Materials, *Chem. Rev.*, 2016, **116**, 962–1052.
  - 44 P. Lova, V. Grande, G. Manfredi, M. Patrini, S. Herbst, F. Würthner and D. Comoretto, All-Polymer Photonic Microcavities Doped with Perylene Bisimide J-Aggregates, *Adv. Opt. Mater.*, 2017, **5**, 1700523.
  - 45 C. Kaufmann, W. Kim, A. Nowak-Król, Y. Hong, D. Kim and F. Würthner, Ultrafast Exciton Delocalization, Localization, and Excimer Formation Dynamics in a Highly Defined Perylene Bisimide Quadruple  $\pi$ -Stack, *J. Am. Chem. Soc.*, 2018, **140**, 4253–4258.
  - 46 J. Sung, A. Nowak-Król, F. Schlosser, B. Fimmel, W. Kim, D. Kim and F. Würthner, Direct Observation of Excimer-Mediated Intramolecular Electron Transfer in a Cofacially-Stacked Perylene Bisimide Pair, *J. Am. Chem. Soc.*, 2016, **138**, 9029–9032.
  - 47 J. Sung, P. Kim, B. Fimmel, F. Würthner and D. Kim, Direct observation of ultrafast coherent exciton dynamics in helical  $\pi$ -stacks of self-assembled perylene bisimides, *Nat. Commun.*, 2015, **6**, 8646.
  - 48 A. Nowak-Król, B. Fimmel, M. Son, D. Kim and F. Würthner, Photoinduced electron transfer (PET) versus excimer formation in supramolecular p/n-heterojunctions of perylene bisimide dyes and implications for organic photovoltaics, *Faraday Discuss.*, 2015, **185**, 507–527.

- 49 B. M. Savoie, N. E. Jackson, L. X. Chen, T. J. Marks and M. A. Ratner, Mesoscopic Features of Charge Generation in Organic Semiconductors, *Acc. Chem. Res.*, 2014, **47**, 2545–2557.
- 50 P. Deria, J.-H. Olivier, J. Park and M. J. Therien, Potentiometric, Electronic, and Transient Absorptive Spectroscopic Properties of Oxidized Single-Walled Carbon Nanotubes Helically Wrapped by Ionic, Semiconducting Polymers in Aqueous and Organic Media, *J. Am. Chem. Soc.*, 2014, **136**, 14193–14199.
- 51 M. Cardona Claudia, W. Li, E. Kaifer Angel, D. Stockdale and C. Bazan Guillermo, Electrochemical Considerations for Determining Absolute Frontier Orbital Energy Levels of Conjugated Polymers for Solar Cell Applications, *Adv. Mater.*, 2011, **23**, 2367–2371.
- 52 V. Lin, S. DiMugno and M. Therien, Highly conjugated, acetylenyl bridged porphyrins: new models for light-harvesting antenna systems, *Science*, 1994, **264**, 1105–1111.
- 53 P. Deria, J. Yu, R. P. Balaraman, J. Mashni and S. N. White, Topology-dependent emissive properties of zirconium-based porphyrin MOFs, *Chem. Commun.*, 2016, **52**, 13031–13034.
- 54 T. V. Duncan, T. Ishizuka and M. J. Therien, Molecular Engineering of Intensely Near-Infrared Absorbing Excited States in Highly Conjugated Oligo(porphinato)zinc-(Polypyridyl)metal(II) Supramolecules, *J. Am. Chem. Soc.*, 2007, **129**, 9691–9703.
- 55 J.-H. Olivier, Y. Bai, H. Uh, H. Yoo, M. J. Therien and F. N. Castellano, Near-Infrared-to-Visible Photon Upconversion Enabled by Conjugated Porphyrinic Sensitizers under Low-Power Noncoherent Illumination, *J. Phys. Chem. A*, 2015, **119**, 5642–5649.
- 56 J. Rawson, A. C. Stuart, W. You and M. J. Therien, Tailoring Porphyrin-Based Electron Accepting Materials for Organic Photovoltaics, *J. Am. Chem. Soc.*, 2014, **136**, 17561–17569.
- 57 J. Park, T.-H. Park, L. E. Sinks, P. Deria, J. Park, M.-H. Baik and M. J. Therien, Unusual solvent polarity dependent excitation relaxation dynamics of a bis[*p*-ethynyl-dithiobenzoato]-Pd-linked bis[(porphinato)zinc] complex, *Mol. Syst. Des. Eng.*, 2018, **3**, 275–284.
- 58 S. Mathew, A. Yella, P. Gao, R. Humphry-Baker, B. F. E. Curchod, N. Ashari-Astani, I. Tavernelli, U. Rothlisberger, M. K. Nazeeruddin and M. Grätzel, Dye-sensitized solar cells with 13% efficiency achieved through the molecular engineering of porphyrin sensitizers, *Nat. Chem.*, 2014, **6**, 242.
- 59 J. A. A. W. Elemans, R. van Hameren, R. J. M. Nolte and A. E. Rowan, Molecular Materials by Self-Assembly of Porphyrins, Phthalocyanines, and Perylenes, *Adv. Mater.*, 2006, **18**, 1251–1266.
- 60 S. Ogi, V. Stepanenko, J. Thein and F. Würthner, Impact of Alkyl Spacer Length on Aggregation Pathways in Kinetically Controlled Supramolecular Polymerization, *J. Am. Chem. Soc.*, 2016, **138**, 670–678.
- 61 *Supramolecular Polymers*, ed. A. Ciferri, Taylor & Francis, Durham, NC, 2nd edn, 2005.
- 62 T. F. A. De Greef, M. M. J. Smulders, M. Wolfs, A. P. H. J. Schenning, R. P. Sijbesma and E. W. Meijer, Supramolecular Polymerization, *Chem. Rev.*, 2009, **109**, 5687–5754.
- 63 X. Zhang, Z. Chen and F. Würthner, Morphology Control of Fluorescent Nanoaggregates by Co-Self-Assembly of Wedge- and Dumbbell-Shaped Amphiphilic Perylene Bisimides, *J. Am. Chem. Soc.*, 2007, **129**, 4886–4887.
- 64 E. Kossov, H. Weissman and B. Rybtchinski, Bending Nanofibers into Nanospirals: Coordination Chemistry as a Tool for Shaping Hydrophobic Assemblies, *Chem. – Eur. J.*, 2014, **21**, 166–176.
- 65 K.-I. Goto, T.-H. Yu, J. Wu, C. H. Diaz and J. P. Colinge, Mobility and screening effect in heavily doped accumulation-mode metal-oxide-semiconductor field-effect transistors, *Appl. Phys. Lett.*, 2012, **101**, 073503.
- 66 S. Wang, X. L. Liang, Q. Chen, Z. Y. Zhang and L. M. Peng, Field-Effect Characteristics and Screening in Double-Walled Carbon Nanotube Field-Effect Transistors, *J. Phys. Chem. B*, 2005, **109**, 17361–17365.
- 67 R. Martel, T. Schmidt, H. R. Shea, T. Hertel and P. Avouris, Single- and multi-wall carbon nanotube field-effect transistors, *Appl. Phys. Lett.*, 1998, **73**, 2447–2449.